Nano Research

ISSN 1998-0124 CN 11-5974/O4
https://doi.org/10.26599/NR.2026.94908671

Research Article

Scalable fiber-skeleton-reinforced graphene-assembled films enabling wash-durable wearable heating

Hao Yuan[1,2,§], Pengfei Chen[1,2,3,§], Xun Li[1,2,§], Xiaoxi Xu[1,2], Wei Qian[2], Huazhang Zhang[2], Zhe Wang[2,4], Huaqiang Fu[1,2], Dingsheng Wang[5](✉), Daping He[1,2,3](✉)

[1] School of Materials Science and Engineering, Wuhan University of Technology, Wuhan 430070, China

[2] Hubei Engineering Research Center of Radio Frequency Microwave Technology and Application, School of Physics and Mechanics, Wuhan University of Technology, Wuhan 430070, China

[3] State Key Laboratory of Silicate Materials for Architectures, Wuhan University of Technology, Wuhan 430070, China

[4] State Key Laboratory of Advanced Technology for Materials Synthesis and Processing, Wuhan University of Technology, Wuhan 430070, China

[5] Department of Chemistry, Tsinghua University, Beijing 100084, China

[§] Hao Yuan, Pengfei Chen, and Xun Li contributed equally to this work.

Nano Res., **Just Accepted Manuscript** • https://doi.org/10.26599/NR.2026.94908671

https://www.sciopen.com/journal/1998-0124 on Mar. 22, 2026

Nano Research

Open Access

Research Article

Scalable fiber-skeleton-reinforced graphene-assembled films enabling wash-durable wearable heating

Hao Yuan[1,2,§], Pengfei Chen[1,2,3,§], Xun Li[1,2,§], Xiaoxi Xu[1,2], Wei Qian[2], Huazhang Zhang[2], Zhe Wang[2,4], Huaqiang Fu[1,2], Dingsheng Wang[5,✉], and Daping He[1,2,3,✉]

[1] *School of Materials Science and Engineering, Wuhan University of Technology, Wuhan 430070, China*
[2] *Hubei Engineering Research Center of Radio Frequency Microwave Technology and Application, School of Physics and Mechanics, Wuhan University of Technology, Wuhan 430070, China*
[3] *State Key Laboratory of Silicate Materials for Architectures, Wuhan University of Technology, Wuhan 430070, China*
[4] *State Key Laboratory of Advanced Technology for Materials Synthesis and Processing, Wuhan University of Technology, Wuhan 430070, China*
[5] *Department of Chemistry, Tsinghua University, Beijing 100084, China*
[§] *Hao Yuan, Pengfei Chen, and Xun Li contributed equally to this work.*

Received: 6 February 2026; **Revised:** 19 March 2026; **Accepted:** 22 March 2026

✉Address correspondence to Dingsheng Wang. wangdingsheng@mail.tsinghua.edu.cn; Daping He. hedaping@whut.edu.cn

Cite this article: *Nano Research*, 2026, 19, 94908671 https://doi.org/10.26599/NR.2026.94908671

ABSTRACT: Wearable heating is a compelling solution for personal thermal management (PTM), enabling localized, energy-efficient warming. Graphene-assembled films (GAFs) possess outstanding flexibility and electrothermal performance, yet their practical application is hindered by inherent brittleness and low resistance to crack propagation, leading to premature mechanical failure and performance drift. Herein, we report a scalable fiber-skeleton-reinforcing strategy for toughening GAFs that addresses this durability bottleneck. Polyacrylonitrile fibers are introduced into the precursor suspension and, after high-temperature treatment, transform into graphitized carbon fibers that stitch graphene layers into a continuous load-bearing network. This fiber-reinforced architecture increases tensile toughness by approximately 90% while preserving high electrical conductivity (0.4×10^6 S/m) and thermal conductivity [1.0×10^3 W/(m·K)]. Integrated into a winter jacket, the film delivers rapid, low-voltage wearable heating, reaching 40.8 °C within 30 s at only 5 V. Critically, the heating performance remains stable after 60 machine-washing cycles, demonstrating a practical pathway toward mass-produced, wash-durable graphene heaters for advanced PTM.

KEYWORDS: Type keywords (4 to 6 keywords) here. The font is Arial 9.

1. Introduction

Personal thermal management (PTM) has become an effective approach to maintain stable thermal comfort and physiological safety under dynamic and extreme environments by providing localized, on-body temperature regulation [1-4]. Among various PTM technologies, wearable electrically heated clothing, which utilizes Joule heating to provide controllable, on-demand warmth, is particularly appealing for cold-weather protection [5, 6]. For such applications, electrothermal materials are required to possess both high Joule heating efficiency and textile-like characteristics, such as lightweight, flexibility, and mechanical durability, to accommodate human body movement and withstand repeated washings [7-10].

Conventional wearable heating elements have predominantly relied on metal-based materials, such as nickel-chromium alloys or copper heating wires [11, 12]. Although these materials exhibit effective heating ability, they suffer from high density, inherent rigidity, and susceptibility to fatigue fracture under repeated deformation. Moreover, the one-dimensional heating geometry of metal wires often results in uneven temperature distribution, which compromises thermal comfort and increases the risk of local overheating. To overcome these limitations, extensive efforts have been devoted to developing flexible electrothermal materials to replace the rigid and heavy metal wires. Representative alternatives include silver nanowire networks [13, 14], MXenes [15-18], conductive polymers and composites [19-21], as well as carbon-based materials ranging from carbon fibers, nanotubes, and laser-induced graphene to graphene-assembled films (GAFs) [22-26]. Among these, the GAFs are regarded as particularly promising owing to their combined properties of low mass, high flexibility, excellent electrical and thermal conductivity, and fast thermal response [27-30].

Nevertheless, the practical use of GAFs as heating elements in wearable devices, especially in electrically heated clothing, requires sufficient mechanical reliability under practical service conditions. While monolayer graphene exhibits extraordinary intrinsic mechanical properties, with a tensile strength of around 130 GPa [31], the mechanical performance of their macroscopic assemblies degrades significantly. Graphene-assembled structures are typically fabricated through vacuum filtration,

coating, or wet spinning of graphene oxide precursors, resulting in a layered architecture formed by stacked nanosheets [32-35]. In such structures, the layers are primarily connected through weak physical interactions [36, 37]. As a result, conventional GAFs often exhibit inherent brittleness and poor resistance to crack propagation, leading to early structural failure. This deficiency in macroscopic mechanical robustness has become a critical bottleneck that restricts the practical deployment of graphene-assembled materials in wearable applications [38-40].

In this work, we report a fiber-skeleton-reinforcing strategy to overcome the mechanical fragility inherent to conventional GAFs. Specifically, we incorporate polyacrylonitrile (PAN) fibers into the precursor suspension. After high-temperature graphitization, these PAN fibers convert into graphitized carbon fibers that help to mechanically reinforce the films. Notably, the processing route is fully compatible with large-scale manufacturing. The resulting films achieve significantly enhanced mechanical toughness without compromising their electrothermal properties. The practical applicability of these fiber-toughened GAFs is demonstrated through their integration into electrically heated clothing, which provides reliable thermal protection in cold environments and excellent resistance to repeated washing.

fiber-skeleton-reinforced GAFs are schematically illustrated in Fig. 1a. Graphene oxide nanoplatelets (GO NPs) are first co-dispersed with polyacrylonitrile (PAN) to form a homogeneous suspension, which enables the assembly of a continuous layered precursor film with intimate GO NP-polymer contact. Subsequent high-temperature graphitization (2850 °C) converts the GO framework into highly ordered graphitic lamellae, while PAN is transformed into graphitized carbon fibers distributed across the interlayers. We explored heat-treatment temperatures to optimize graphitization and electrical properties (Figs. S1 and S2). The post-rolling step densifies the film at the macroscopic level, suppresses interfacial voids, and promotes in-plane alignment of graphitic layers, thereby maximizing load transfer and maintaining a compact, conductive architecture.

From a mechanical perspective, the PAN-derived carbon fibers act as interlamellar bridging components that locally anchor adjacent graphitic sheets and increase resistance to layer slippage under bending. As depicted in Fig. 1b, these bridges help redistribute strain and mitigate interlayer delamination,

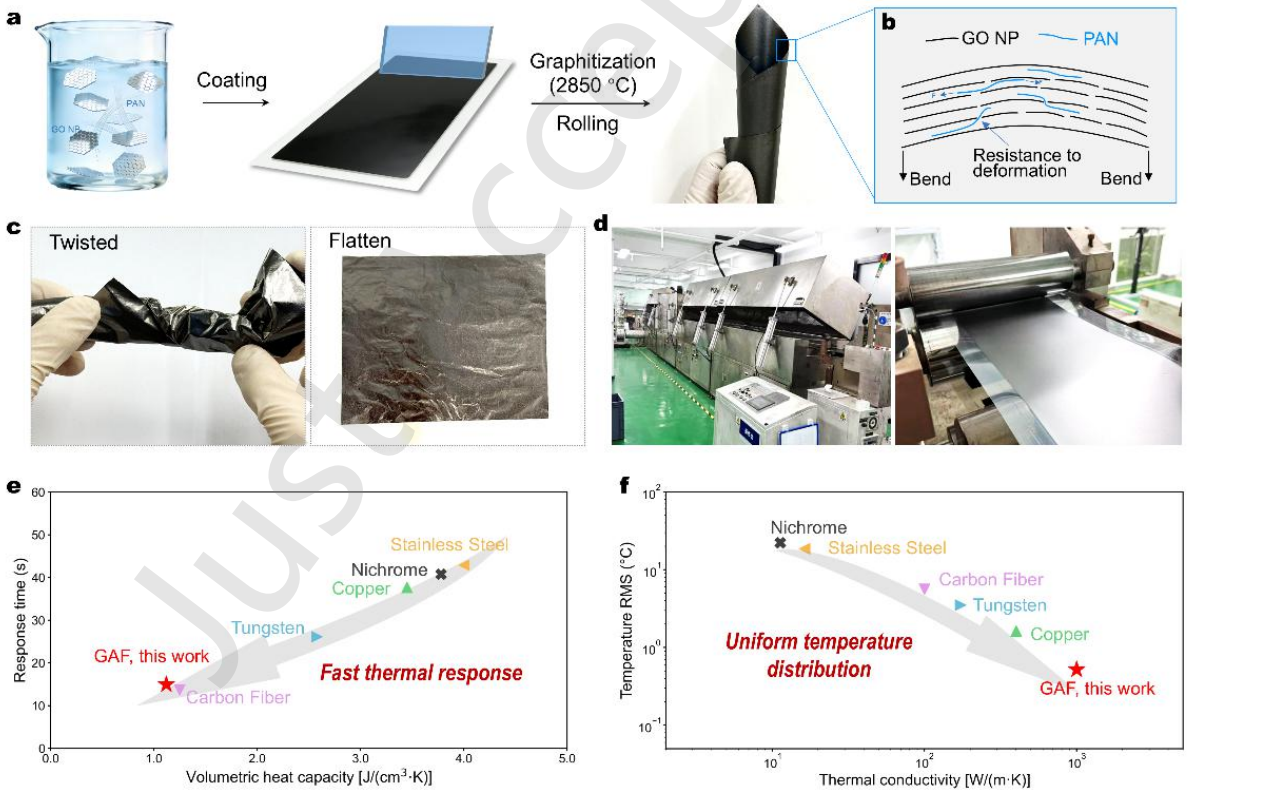

Figure 1. Scalable fabrication and performance advantages of GAFs. (a) Schematic illustration of the fabrication process of GAFs. (b) Schematic illustrating the architecture of the fiber-skeleton-reinforcing method. (c) Photographs of a GAF twisted (left) and subsequently flattened (right). (d) Photographs of the large-scale production line. Finite-element calculation results showing (e) thermal response time plotted against volumetric heat capacity, and (f) temperature distribution non-uniformity [characterized by root-mean-square (RMS) of temperature distribution] plotted against thermal conductivity, comparing GAFs with representative electrothermal materials.

2. Results and discussion

2.1. Scalable fabrication and performance advantages

The fabrication process and structural design concept of the

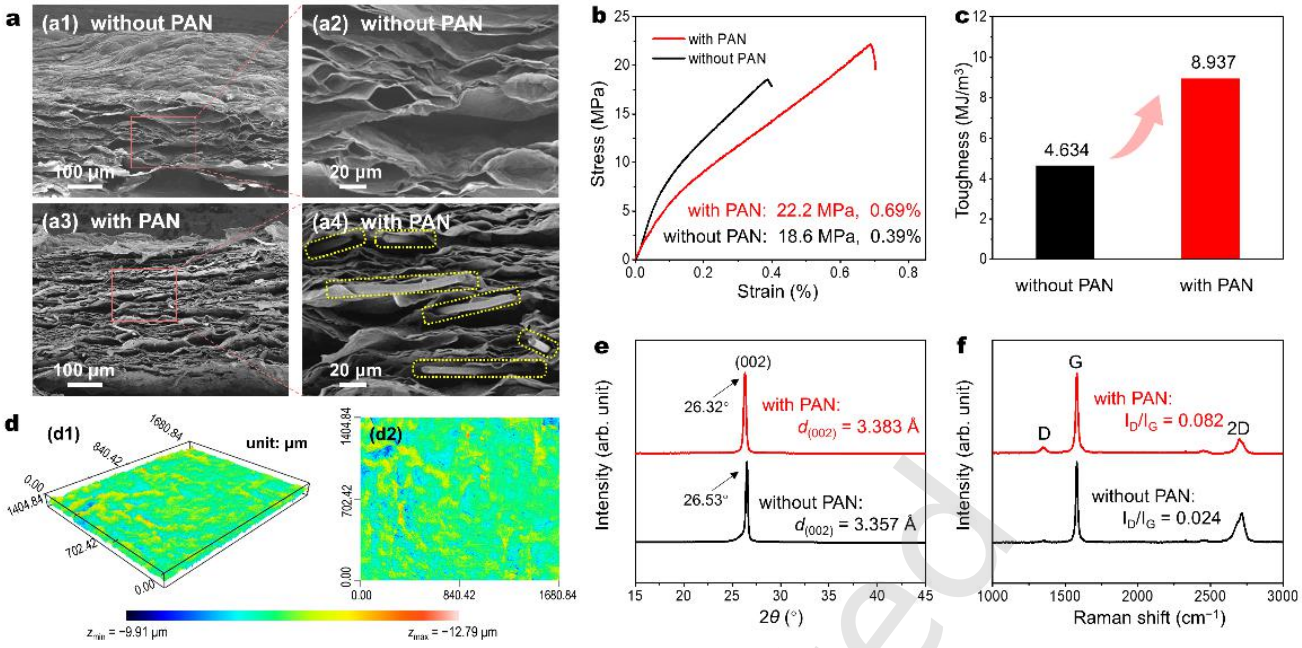

Figure 2. Mechanical reinforcement and structural characterization of the GAFs. (a) Cross-sectional SEM images of the GAF without PAN fibers (a1, a2) and the fiber-reinforced GAF (a3, a4) before rolling compression. The yellow dotted lines in (a4) highlight the graphitized PAN fibers intercalated between graphene layers. (b) Typical tensile stress-strain curves of the films. (c) Comparison of tensile toughness of the GAF without PAN fibers and the fiber-reinforced GAF. (d) Surface morphology characterization of the fiber-reinforced GAF. (e) XRD patterns and (f) Raman spectra of the GAFs with and without PAN fiber addition.

leading to enhanced deformation tolerance without sacrificing the intrinsic advantages of a laminated graphite structure. Overall, this design couples highly aligned graphitic transport pathways with interlayer reinforcement, offering a robust route toward flexible, mechanically reliable GAFs for wearable and deformable electronics.

As shown in Fig. 1c, the film can be severely deformed (twisted) and then fully flattened without catastrophic cracking, indicating a damage-tolerant laminated architecture that is compatible with repeated folding and handling in actual garments. This exceptional bend tolerance and structural robustness are prerequisites for wearable applications, ensuring the heating element can seamlessly conform to the complex curvature of the human body and withstand mechanical deformations during daily movements.

Fig. 1d not only demonstrates the scalability of GAF production, but also implies a key manufacturing advantage for wearable heaters: the continuously fabricated film is inherently compatible with roll-to-roll patterning and device integration. In practice, the large-area GAFs can be directly fed into continuous processes, such as laser scribing/cutting, mask-based patterning, or lamination-assisted shaping, to define heater geometries efficiently. This roll-to-roll-compatible workflow enables rapid and demand-driven customization of wearable heating elements, allowing the same parent film to be transformed into diverse layouts (e.g., serpentine traces, zoned heating patches, or anatomically conformal patterns) tailored to different body parts and heating strategies. Consequently, scalable GAF manufacturing can be coupled with continuous patterning to realize fast prototyping-to-production translation, and to efficiently deliver wearable heating films with application-specific shapes, sizes, and heating zones for varied end-use scenarios.

The as-fabricated GAFs exhibit outstanding electrical and thermal properties which are critical in high-efficiency Joule heating (Table S1). In particular, the electrical conductivity is 0.4×10^6 S/m (in-plane), the thermal conductivity reaches 1.0×10^3 W/(m·K) (in-plane), and the specific heat is as low as 0.8 J/(g·K). Meanwhile, the density of the films 1.4 g/cm^3 is only about 16% that of copper, highlighting a distinct advantage in lightweight designs.

To elucidate how specific physical parameters underpin the superior electrothermal performance of GAFs, finite-element simulations were conducted. As an illustrative comparison, we employed a thin-film geometry model to evaluate the electrothermal responses of different materials under identical heating power and idealized, freestanding thermal boundary conditions (see Figs. S3-S8 for modeling details). As highlighted in Figs. 1e and 1f, the simulation results reveal two key advantages stemming from the superior physical properties of GAFs: (1) their low density and specific heat minimize the volumetric heat capacity, enabling a fast thermal response; and (2) the exceptional thermal conductivity facilitates in-plane heat spreading, ensuring a highly uniform temperature distribution. Collectively, these results establish the GAFs as a rare class of electrothermal film that couples industrial scalability, mechanical deformability, rapid thermal actuation, and spatially uniform heating, which are all essential for reliable, comfortable wearable heaters.

2.2. Mechanical reinforcement via PAN fiber addition

Mechanical robustness is a critical determinant for the applicability of flexible electrothermal films in wearable applications. To address the inherent brittleness of GAFs, we introduce a toughening strategy by incorporating PAN fibers into the precursor suspension. Upon high-temperature treatments,

these PAN fibers are carbonized and graphitized into carbon fibers. The complete elimination of nitrogen and the final chemical state of these graphitized fibers were confirmed by X-ray photoelectron spectroscopy (XPS, Fig. S9). Fig. 2(a) elucidates how these graphitized carbon fibers function as an interlayer reinforcement to simultaneously strengthen the GAFs while largely preserving the graphitic framework. The GAF without PAN fibers exhibits a typical multilayered stacking of graphene nanosheets, with interlayer voids formed by the gasification of oxygen-containing groups during high-temperature treatments. In contrast, the fiber-reinforced GAF features a fibrous morphology intercalated between the graphene stacks, corresponding to the graphitized fibers derived from the PAN precursor. These graphitized fibers, highlighted by yellow dotted lines in Fig. 2(a4), serve as mechanical bridges that facilitate stress transfer and trigger energy-dissipation mechanisms, such as crack bridging and fiber pull-out, that occur during mechanical deformation. These toughening mechanisms are further corroborated by direct microscopic observations of the post-tensile fracture surfaces (Fig. S10), which clearly display the pulled-out graphitized carbon fibers bridging the fractured graphene layers.

Tensile tests confirm that this fiber-reinforcement strategy significantly enhances the mechanical robustness of GAFs. As shown in the stress-strain curves in Fig. 2b, the tensile strength and elongation at break increased from 18.6 MPa and 0.39% for the pure GAFs to 22.2 MPa and 0.69% for the fiber-reinforced GAFs, respectively. Consequently, the tensile toughness exhibited a substantial improvement of approximately 90%, rising from 4.634 MJ/m^3 to 8.937 MJ/m^3 (Fig. 2c). This toughening effect is attributed to the incorporated fibers acting as bridges across micro-cracks, effectively suppressing crack propagation. The frictional sliding and subsequent pull-out of fibers from the graphene matrix dissipate significant fracture energy, thereby enhancing the toughness [41-43].

Crucially, this mechanical reinforcement was achieved without compromising the high structural integrity and the overall graphitic nature of GAFs. As shown in Fig. 2d, the compressed film maintains a high degree of flatness with a root-mean-square (RMS) surface roughness of about Sq = 1.66 μm, suggesting a highly ordered internal alignment. The XRD patterns in Fig. 2e demonstrate high crystallinity in both GAFs with and without PAN addition. The fiber-reinforced GAF shows a slightly increased interlayer spacing ($d_{(002)}$ = 3.383 Å vs 3.357 Å without PAN), which is primarily driven by the local steric hindrance introduced by the intercalated carbon phases at the atomic scale. This local perturbation of the parallel stacking is also supported by the broader azimuthal diffraction distribution observed in small-angle X-ray scattering (SAXS, Fig. S11). Importantly, this atomic-scale layer expansion physically coexists with the macroscopic and mesoscopic densification achieved through rolling compression. Furthermore, the Raman spectra (Fig. 2f) display typical graphitic features [44]. Although the I_D/I_G ratio increased slightly from 0.024 to 0.082 after PAN addition, it remains at a very low level. This can be reasonably attributed to interfacial interactions and the incorporation of graphitized PAN domains. Meanwhile, the nominal crystalline size along the a-axis (L_a) can be calculated from the I_D/I_G ratio using the following equation [45]:

$$L_a = (2.4 \times 10^{-10}) \times \lambda_1^4 \times (I_G/I_D)$$

where λ_1 represents the Raman laser wavelength of 532 nm. The GAFs before and after the fiber reinforcing show comparable L_a of 801.0 nm and 234.4 nm, respectively. This change mainly reflects an ensemble averaging effect during the Raman measurement. Because the micrometer-scale laser spot simultaneously probes the highly ordered graphene matrix and the relatively more defective graphitized carbon fibers, the resulting signal represents the average structural state of the mixed composite, rather than indicating that the intrinsic long-range crystalline order of the graphene framework was destroyed. Together, these results support a reinforcement picture in which PAN-derived graphitic fibers act as the interlayer "skeleton", delivering a marked toughness gain while maintaining the essential graphitic framework required for high-performance functional films [46].

2.3. Joule heating characteristics of GAF

To assess the potential of GAFs in electrothermal applications, their Joule heating characteristics are systematically investigated. For pure resistive Joule heating, the fundamental electrical-to-thermal energy conversion approaches 100%. Therefore, we primarily evaluate the practical heating efficacy through saturation temperature and thermal response time, as any apparent system-level efficiency strongly depends on external measurement configurations and heat dissipation. Under a constant bias of 5.0 V (Fig. 3a), the surface temperature increases rapidly in the first tens of seconds, as captured by the infrared snapshots, and then gradually approaches a steady plateau of about 102 ± 3 °C. The thermal response time, defined as the time required for the temperature to reach 63.2% of the maximum temperature increase, is roughly estimated to be about 17 ± 1 s. This transient-to-steady evolution suggests efficient electrical-to-thermal conversion together with a relatively small thermal mass, allowing the heater to reach the targeted temperature quickly. Once the voltage is turned off, the temperature decays sharply, indicating minimal thermal inertia and confirming a reversible, switchable heating mode, which is suitable for on-demand comfort management and intermittent operation. The inset infrared thermal images reveal a uniform temperature distribution across the heating area throughout the heating and cooling phases, indicating homogeneous film quality. Furthermore, the curve maintains a stable plateau during operation, demonstrating excellent operational stability.

The voltage-dependent heating profiles (Fig. 3b) show that the steady-state temperature can be continuously tuned by varying the applied voltage from 2.0 to 7.0 V, covering the practical operating range compatible with compact, battery-powered supplies. The saturation temperature (T_{sat}) increases monotonically with the increase of voltage. Fig. 3c plots T_{sat} as a function of the square of the applied voltage (U^2). The data exhibits a linear relationship (R^2 = 0.9892), which is consistent

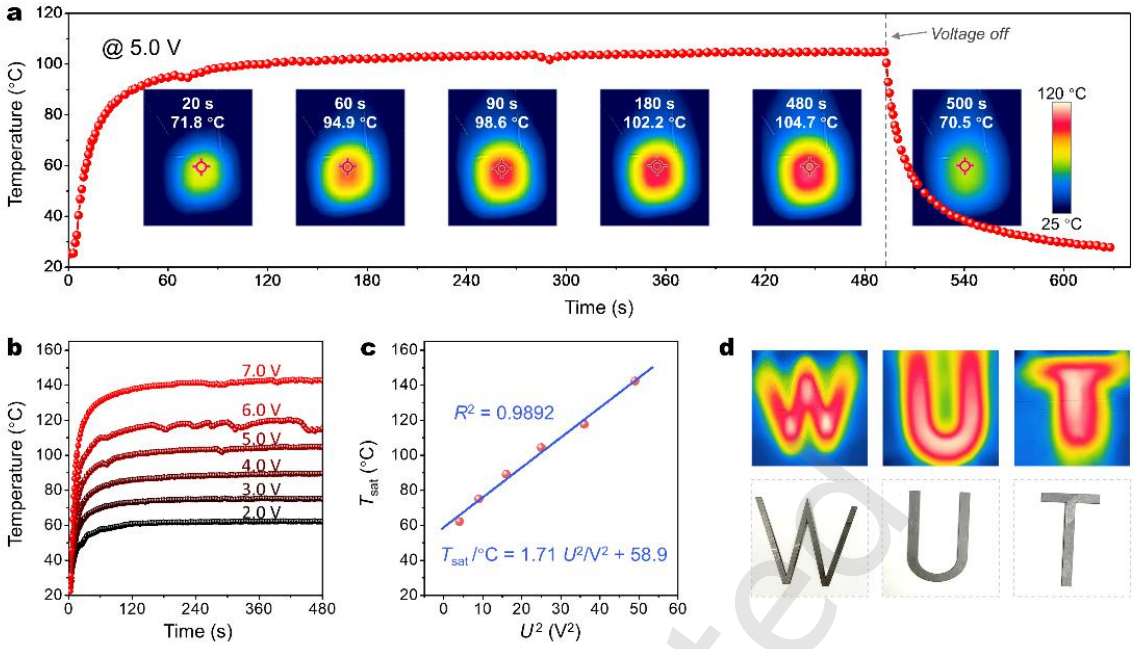

Figure 3. Electrothermal performance and patterning capability of GAFs. (a) Time-dependent surface temperature profile of a GAF at voltage of 5.0 V. Insets shows the corresponding infrared thermal images at different stages. (b) Temperature evolution curves under various applied voltages ranging from 2.0 to 7.0 V. (c) The plot of saturation temperature (T_{sat}) versus the square of applied voltage (U^2), revealing a linear relationship within the applied voltage range. (d) Infrared thermal images (top) and the corresponding photographs (bottom) of GAFs cut into letters "W", "U" and "T".

with the combined effects of Joule's law (heat generation proportional to U^2) and Newton's law of cooling (heat dissipation linearly dependent on temperature difference), as T_{sat} is established at the balance between heat generation and dissipation. This linear relationship indicates that the heat generation of GAFs can be precisely controlled by regulating the applied voltage, implying that the thermal output can be quantitatively programmed and predicted, facilitating straightforward voltage-based control and offering a solid basis for integrating temperature feedback loops in wearable electronics.

In practical electrothermal applications, customizing the operating voltage and heating power is often required. If the electrical conductivity of the electrothermal film is given, this can be most effectively achieved by designing the geometry (i.e., shape, pattern, and size) of the heating element to control its electrical resistance. Our GAFs demonstrate exceptional processability and can be readily patterned into custom shapes using simple methods such as mechanical cutting or laser engraving [47]. Fig. 3d shows digital photographs and corresponding infrared thermal images of GAFs cut into the letters "W", "U", and "T". The distinct shapes exhibit uniform heating without hot spots at the edges or corners, validating the structural integrity of the film after cutting. This easy patterning capability not only allows precise design of operating voltage and heating power (more examples given in Supplementary Section S4), but also enables the fabrication of complex heating patterns to meet specific application demands.

2.4. Application in heated clothing and washability

To demonstrate the practical application of the fiber-toughened GAFs in personal thermal management, we developed electrically heated clothing designed for cold protection (Fig. 4a). Several heating elements were embedded into a commercial winter jacket. Each heating element consists of a tri-layered sandwich structure, in which a patterned GAF layer is encapsulated between two polyimide (PI) films. The PI encapsulation is employed to provide electrical insulation, waterproofing, and mechanical protection. The central GAF layer is patterned to tailor its electrical resistance, which allows for the customization of operating voltage and power density. This design ensures that the generated heat is sufficient for human warmth in cold environments while avoiding overheating. Thus, when powered by a portable battery, the clothing provides on-demand heating.

Fig. 4b shows the digital photographs of the heating element. When held by hand, the element exhibits a natural droop, demonstrating its excellent flexibility. Therefore, the integration of these heating elements into the clothing does not compromise wearing comfort or restrict human movement. Fig. 4c presents the photograph and the corresponding infrared thermal image of the heated clothing during operation. Upon turning on the power, the uniform heat is generated across the targeted areas [48, 49]. As shown in Fig. 4d, at a safe voltage of 5.0 V, the system exhibits a rapid thermal response: the temperature rises to 36.2 °C, close to human body temperature, within just 10 s, and reaches a stable equilibrium temperature of 40.8 °C within 30 s. This rapid heating capability is essential for providing immediate thermal relief in cold conditions.

Notably, the incorporation of PAN fibers significantly enhances the durability of the heating elements during repeated washing. For the washability test, the battery was removed, and the heating elements remained in the jacket during machine washing cycles. During repeated washing, the complex bending and shear stresses progressively induce micro-cracks within the

conductive film, leading to a sudden open-circuit failure once the accumulated damage reaches a critical level. The incorporated fiber skeleton effectively slows down the initiation and propagation of these micro-cracks. Because the heating film is permanently sealed within the PI layers to ensure waterproofing, stripping the encapsulation for intermediate microscopic observation would inevitably destroy the structural integrity and the original failure state. Therefore, operating current serves as a reliable indicator of the sustained performance of the heating devices. As shown in Fig. 4e, the operating current of the fiber-reinforced GAF heating element remained stable for over 60 washing cycles, indicating robust structural integrity. In contrast, the control sample without PAN fibers completely failed after only 33 wash cycles. This result clearly demonstrates the effectiveness of the fiber-toughening strategy in enhancing the resistance to repeated washing, thereby solving the key bottleneck in the longevity of GAFs as heating elements in wearable devices.

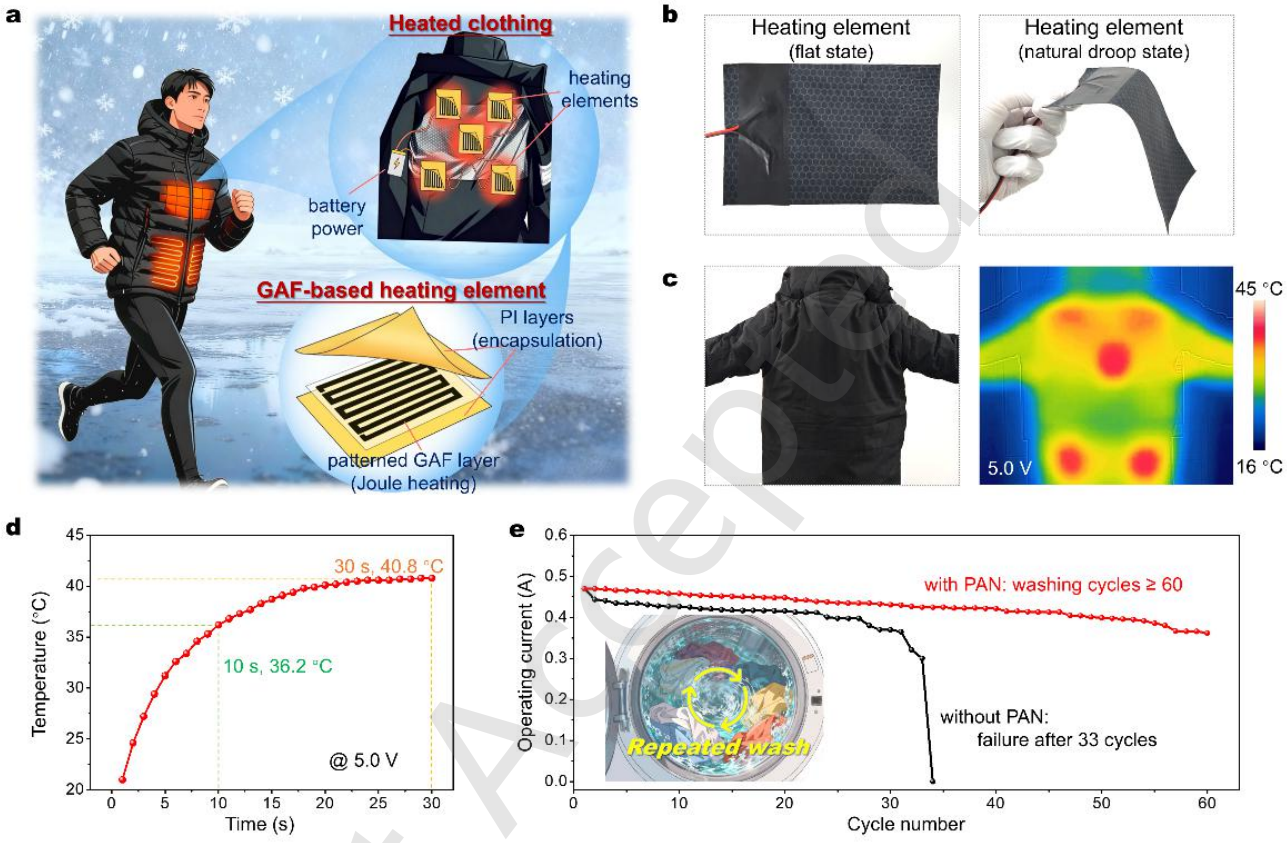

Figure 4. Application of GAF in heated clothing. (a) Schematic illustration of the heated clothing system and the tri-layered heating element consisting of patterned GAF encapsulated by PI films. (b) Photographs of the heating element in a flat state (left) and a naturally drooping state (right). (c) Optical photograph and corresponding infrared thermal image of the heated clothing worn by a human. (d) Time-dependent temperature curve of the heating element embedded in jacket. (e) Durability of the heating elements during repeated machine-washing cycles.

3. Conclusion

In summary, we have developed a scalable strategy to fabricate fiber-toughened GAFs that overcome the mechanical fragility and ensure durability for wearable applications. By incorporating PAN-derived graphitized fibers, the GAFs achieve nearly 90% enhancement in toughness, without compromising their electrothermal performance. The practical applicability of these films is demonstrated through electrically heated clothing, which delivers rapid, uniform, and controllable warmth suitable for cold-weather protection. Most significantly, the heating elements based on fiber-toughened GAFs exhibited outstanding durability, maintaining stable performance even after 60 machine-washing cycles. This work provides a feasible route for the mass production of robust flexible heaters for advanced personal thermal management.

4. Methods

4.1. Materials

GO filter cake was purchased from the Wuxi Chengyi Education Technology Co., Ltd. The elemental composition was analyzed by energy dispersive spectroscopy as mainly C 58.08% and O 40.21%, with trace amounts of S and Cl. PAN fibers were purchased from the Shaoxing Jiema Composite Materials Co., Ltd. The average diameter of the PAN fibers is ~35 μm. All raw materials and reagents were used without additional purification.

4.2. Fabrication of graphene assembled films

The GAFs were fabricated from GO by a high-temperature graphitization process. First, the 3 wt.% GO aqueous suspension was mixed with PAN fibers at a mass ratio of GO:PAN = 4:1. To improve the dispersion of the fibers and stabilize the GO sheets, 25 wt.% ammonia water was added at a volume ratio of 2.4 mL per 100 mL of suspension. The mixture was then coated onto a clean glass substrate using a doctor blade casting method with a wet film thickness of 4 mm and dried at 55 °C for 12 h.

Subsequently, these precursor films were subjected to high-temperature treatments, including stabilization at 300 °C in air for 1 h, followed by carbonization at 1500 °C and graphitization at 2850 °C. Finally, rolling compression (3 MPa, 6 passes) was applied to eliminate internal micro-voids, yielding compact GAFs.

4.3. Fabrication of GAF-based heating element

To match the power requirements for use in heated clothing, the GAFs were patterned into designed geometries via laser engraving. The heating element was then fabricated by sandwiching the patterned GAFs between two PI layers. Specifically, the patterned GAFs were placed onto a bottom PI layer and connected to copper foil electrodes using silver paste. The assembly was then encapsulated by thermally laminating a top PI layer using a flat heat press at 150 °C under ~1.2 MPa for 3 min, yielding the final heating element.

4.4. Characterizations

The micromorphology of GAFs was characterized using a field-emission scanning electron microscope (FESEM, JSM-7610F Plus, JEOL). The crystal structures were analyzed using an X-ray diffractometer (XRD, Rigaku Smartlab) with Cu Kα radiation (λ = 1.5406 Å). The graphitic structures were characterized using a Raman spectrometer (DXR3, Thermo Fisher Scientific). The surface roughness was quantified using a 3D optical profilometer (ContourGT-X3, Bruker). Electrical conductivity was determined with a four-point probe resistivity tester (RTS-8, Four Probes Tech). Mechanical properties were measured using a universal testing machine (Instron 5848) at a crosshead speed of 0.4 mm/min. Tensile specimens were prepared in a standard dumbbell shape with a gauge length of 50 mm and a width of 5 mm. The in-plane thermal conductivity (k) was calculated using $k = \alpha \times \rho \times C_p$, where the thermal diffusivity (α) was measured using laser flash analysis (LFA 467, Netzsch), and the specific heat capacity (Cp) was obtained from differential scanning calorimetry (DSC, Q2000). For Joule-heating experiments, a programmable DC power source with auto-ranging capability (IT6953A, Itech Electronic) was used to supply the electrical input, while the surface temperature evolution was monitored by an infrared thermal imager (ST9450, Wanchuang).

Electronic Supplementary Material: Supplementary material (Fig. S1-S13, Table S1 and S2) is available in the online version of this article at https://doi.org/10.26599/NR.2026.94908671.

Data availability

All data needed to support the conclusions in the paper are presented in the manuscript and the Electronic Supplementary Material. Additional data related to this paper may be requested from the corresponding author upon request.

Acknowledgements

This work was supported by the National Natural Science Foundation of China (22279097, 5250021087), the Natural Science Foundation of Hubei Province (2025AFB038, 2025AFD120), the China Postdoctoral Science Foundation (2024M762511), the joint funding by the China Postdoctoral Science Foundation and Hubei Province (2025T015HB), and the Fundamental Research Funds for the Central Universities (104972025RSCbs0021, 104972025RSCbs0153).

Declaration of competing interest

All the contributing authors report no conflict of interests in this work.

Author contribution statement

H.Y.: Conceptualization, Data curation, Formal analysis, Investigation, Writing - original draft. P.C.: Conceptualization, Data curation, Formal analysis, Methodology, Validation, Writing - original draft. X.L.: Data curation, Investigation, Validation, Writing - original draft. X.X.: Conceptualization, Formal analysis, Validation, Writing - review & editing. W.Q.: Data curation, Investigation, Writing - review & editing. H.Z.: Writing - review & editing. Z.W.: Writing - review & editing. H.F.: Writing - review & editing. D.W.: Conceptualization, Supervision, Writing - review & editing. D.H.: Conceptualization, Funding acquisition, Supervision, Writing - review & editing. All the authors have approved the final manuscript.

Use of AI statement

None.

References

[1] Hsu, P.-C.; Song, A. Y.; Catrysse, P. B.; Liu, C.; Peng, Y.; Xie, J.; Fan, S.; Cui, Y. Radiative human body cooling by nanoporous polyethylene textile. *Science* **2016**, 353, 1019-1023.

[2] Peng, Y.; Cui, Y. Advanced textiles for personal thermal management and energy. *Joule* **2020**, 4, 724-742.

[3] Ding, C.; Gao, P.; Wang, X.; Yin, X.; Yu, J.; Ding, B. Multimodal super-cooling textiles for all-scenario passive hygrothermal comfort. *Adv. Mater.* **2025**, 37, 2417022.

[4] Faruk, O.; Ahmed, A.; Khadem, A. H.; Jia, L.; Sun, L. Graphene-functionalized textile composites for wearable Joule heating applications. *Adv. Nanocompos.* **2025**, 2, 108-123.

[5] Wang, J.; Ju, X.; Wang, M.; Zhu, Y.; Chong, A.; Fan, Y.; Cao, B. Alternating intermittent heating: An energy-efficient wearable heating strategy for enhanced comfort in extremely cold environments. *Energy* **2025**, 339, 131234.

[6] Huang, Z.; Li, S.; Guo, H.; Huang, C.; Bian, Y.; Gong, Y.; Huang, J.; Zeng, Q. Multi-scale GO/CNT/AlN nanocomposites for high-performance flexible electrothermal film heaters. *J. Mater. Chem. C* **2023**, 11, 9925-9936.

[7] Sala de Medeiros, M.; Goswami, D.; Chanci, D.; Moreno, C.; Martinez, R. V. Washable, breathable, and stretchable e-textiles wirelessly powered by omniphobic silk-based coils. *Nano Energy* **2021**, 87, 106155.

[8] Ding, Z.; Liu, P.; Xu, K.; Tang, G.; Zhu, C.; Chen, J.; Gao, Q.; Ni, Y.; Hao, Z.; Xu, G.; Liu, F. Facile construction of graphene based ultra folding resistance and high-efficiency electric heating film by multi-molecules induced orientation and interface regulation. *Chem. Eng. J.* **2025**, 508, 152345.

[9] Zuo, X.; Zhang, X.; Qu, L.; Miao, J. Smart fibers and textiles for personal thermal management in emerging wearable applications. *Adv. Mater. Technol.* **2023**, 8, 2201137.

[10] Tian, Y.; Ding, R.; Yoon, S. S.; Zhang, S.; Yu, J.; Ding, B. Recent advances in next-generation textiles. *Adv. Mater.* **2025**, 37, 2417022.

[11] Stoppa, M.; Chiolerio, A. Wearable electronics and smart textiles: A critical review. *Sensors* **2014**, 14, 11957-11992.

[12] Wang, F.; Liu, Y.; Yu, J.; Li, Z.; Ding, B. Recent progress on general wearable electrical heating textiles enabled by functional fibers. *Nano Energy* **2024**, 124, 109497.

[13] Celle, C.; Mayousse, C.; Moreau, E.; Basti, H.; Carella, A.; Simonato, J.-P. Highly flexible transparent film heaters based on random networks of silver nanowires. *Nano Res.* **2012**, 5, 427-433.

[14] Huang, Q.; Shen, W.; Fang, X.; Chen, G.; Guo, J.; Xu, W.; Tan, R.;

Song, W. Highly flexible and transparent film heaters based on polyimide films embedded with silver nanowires. *RSC Adv.* **2015**, 5, 45836-45842.

[15] Liu, L.-X.; Chen, W.; Zhang, H.-B.; Zhang, Y.; Tang, P.; Li, D.; Deng, Z.; Ye, L.; Yu, Z.-Z. Tough and electrically conductive Ti3C2Tx MXene-based core-shell fibers for high-performance electromagnetic interference shielding and heating application. *Chem. Eng. J.* **2022**, 430, 133074.

[16] Zhou, M.; Hu, Y.; Yan, Z.; Fu, H. Flexible MXene-based Janus film with superior heat dissipation capability for ultra-efficient electromagnetic interference shielding and Joule heating. *Carbon* **2024**, 219, 118835.

[17] Li, L.; Cao, Y.; Liu, X.; Wang, J.; Yang, Y.; Wang, W. Multifunctional MXene-based fireproof electromagnetic shielding films with exceptional anisotropic heat dissipation capability and Joule heating performance. *ACS Appl. Mater. Interfaces* **2020**, 12, 27350-27360.

[18] Park, T. H.; Yu, S.; Koo, M.; Kim, H.; Kim, E. H.; Park, J.-E.; Ok, B.; Kim, B.; Noh, S. H.; Park, C.; Kim, E.; Koo, C. M.; Park, C. Shape-adaptable 2D titanium carbide (MXene) heater. *ACS Nano* **2019**, 13, 6835-6844.

[19] Zhou, J.; Mulle, M.; Zhang, Y.; Xu, X.; Li, E. Q.; Han, F.; Thoroddsen, S. T.; Lubineau, G. High-ampacity conductive polymer microfibers as fast response wearable heaters and electromechanical actuators. *J. Mater. Chem. C* **2016**, 4, 1238-1249.

[20] Xu, Y.; Kraemer, D.; Song, B.; Jiang, Z.; Zhou, J.; Loomis, J.; Wang, J.; Li, M.; Ghasemi, H.; Huang, X.; Li, X.; Chen, G. Nanostructured polymer films with metal-like thermal conductivity. *Nat. Commun.* **2019**, 10, 1881.

[21] Wu, X.; Yin, T.; Liu, W.; Wan, L.; Liao, Y. The advances in polymer-based electrothermal composites: A review. *Polymers* **2025**, 17, 2047.

[22] Sui, D.; Huang, Y.; Huang, L.; Liang, J.; Ma, Y.; Chen, Y. Flexible and transparent electrothermal film heaters based on graphene materials. *Small* **2011**, 7, 3186-3192.

[23] Chen, P.; Li, Z.; Chang, Y.; Yang, X.; Jiang, S.; Qian, W.; Li, X.; Yuan, H.; Wang, Z.; Shi, Z.; He, D. Enhancing the conductivity of laser-induced graphene via a facile high-crystallinity-riveting method for multifunctional applications. *ACS Appl. Mater. Interfaces* **2025**, 17, 64771-64782.

[24] Chen, P.; Yang, X.; Chang, Y.; Qian, W.; Fu, H.; Xu, W.; Ren, L.; Wang, Z.; Zu, H.; Wang, D.; He, D. Superior microwave shielding modulation based on rapidly prepared graphene metasurface. *Natl. Sci. Rev.* **2025**, 12, nwaf395.

[25] Meng, X.; Chen, T.; Li, Y.; Liu, S.; Pan, H.; Ma, Y.; Chen, Z.; Zhang, Y.; Zhu, S. Assembly of carbon nanodots in graphene-based composite for flexible electro-thermal heater with ultrahigh efficiency. *Nano Res.* **2019**, 12, 2498-2508.

[26] Zhang, Y.; Ren, H.; Chen, H.; Chen, Q.; Jin, L.; Peng, W.; Xin, S.; Bai, Y. Cotton fabrics decorated with conductive graphene nanosheet inks for flexible wearable heaters and strain sensors. *ACS Appl. Nano Mater.* **2021**, 4, 9709-9720.

[27] Yao, Y.; Fu, K. K.; Yan, C.; Dai, J.; Chen, Y.; Wang, Y.; Zhang, B.; Hitz, E.; Hu, L. Three-dimensional printable high-temperature and high-rate heaters. *ACS Nano* **2016**, 10, 5272-5279.

[28] Hao, Y.; Ming, X.; Lu, J.; Cao, M.; Zhang, P.; Shi, H.; Li, K.; Gao, Y.; Wang, L.; Fang, W.; Chen, Y.; Zhang, L.; Sun, H.; Gao, W.; Liu, Y.; Xu, Z.; Gao, C. Bidirectionally high-thermally conductive and environmentally adaptive graphene thick films enabled by seamless bonding assembly for extreme thermal management. *Adv. Funct. Mater.* **2024**, 34, 2401234.

[29] Li, L.; Yang, J.; Tan, R.; Shu, W.; Low, C. J.; Zhang, Z.; Zhao, Y.; Li, C.; Zhang, Y.; Li, X.; Zhang, H.; Zhao, X.; Kou, Z.; Xiao, Y.; Verpoort, F.; Wang, H.; Mai, L.; He, D. Large-scale current collectors for regulating heat transfer and enhancing battery safety. *Nat. Chem. Eng.* **2024**, 1, 542-551.

[30] Liu, Y.; Li, P.; Wang, F.; Fang, W.; Xu, Z.; Gao, W.; Gao, C. Rapid roll-to-roll production of graphene films using intensive Joule heating. *Carbon* **2019**, 155, 462-468.

[31] Lee, C.; Wei, X.; Kysar, J. W.; Hone, J. Measurement of the elastic properties and intrinsic strength of monolayer graphene. *Science* **2008**, 321, 385-388.

[32] Li, D.; Müller, M. B.; Gilje, S.; Kaner, R. B.; Wallace, G. G. Processable aqueous dispersions of graphene nanosheets. *Nat. Nanotechnol.* **2008**, 3, 101-105.

[33] Wang, Z.; Mao, B.; Zhao, M.; Calatayud, D. G.; Qian, W.; Li, P.; Hu, Z.; Fu, H.; Zhao, X.; Yan, S.; Kou, Z.; He, D. Ultrafast macroscopic assembly of high-strength graphene oxide membranes by implanting an interlaminar superhydrophilic aisle. *ACS Nano* **2022**, 16, 3934-3942.

[34] Dong, L.; Chen, Z.; Zhao, X.; Ma, J.; Lin, S.; Li, M.; Bao, Y.; Chu, L.; Leng, K.; Lu, H.; Loh, K. P. A non-dispersion strategy for large-scale production of ultra-high concentration graphene slurries in water. *Nat. Commun.* **2018**, 9, 745.

[35] Cao, S.; Fu, H.; Chen, P.; Feng, H.; Zhang, Z.; Lin, Z.; Wang, Z.; Qian, W.; Tian, C.; Li, L.; He, D. Weldable graphene foams for wide-range thermal switches. *Cell Rep. Phys. Sci.* **2025**, 6, 101234.

[36] Qian, W.; Fu, H.; Sun, Y.; Wang, Z.; Wu, H.; Kou, Z.; Li, B. W.; He, D.; Nan, C. W. Scalable assembly of high-quality graphene films via electrostatic-repulsion aligning. *Adv. Mater.* **2022**, 34, 2205678.

[37] Xiong, Z.; Shen, L.; Long, J.; Li, X.; Zhou, K.; Choi, G. M.; Ou, K.; Yang, G.; Ma, W.; Lee, H. S.; Sun, Y.; Li, D. Ultrahigh concentration exfoliation and aqueous dispersion of few-layer graphene by excluded volume effect. *Nat. Commun.* **2024**, 15, 1234.

[38] Zhang, Y.; Gong, S.; Zhang, Q.; Ming, P.; Wan, S.; Peng, J.; Jiang, L.; Cheng, Q. Graphene-based artificial nacre nanocomposites. *Chem. Soc. Rev.* **2016**, 45, 2378-2395.

[39] Wen, Y.; Wu, M.; Zhang, M.; Li, C.; Shi, G. Topological design of ultrastrong and highly conductive graphene films. *Adv. Mater.* **2017**, 29, 1702831.

[40] Duan, J.; Gong, S.; Gao, Y.; Xie, X.; Jiang, L.; Cheng, Q. Bioinspired ternary artificial nacre nanocomposites based on reduced graphene oxide and nanofibrillar cellulose. *ACS Appl. Mater. Interfaces* **2016**, 8, 10545-10550.

[41] Wan, S.; Chen, Y.; Fang, S.; Wang, S.; Xu, Z.; Jiang, L.; Baughman, R. H.; Cheng, Q. High-strength scalable graphene sheets by freezing stretch-induced alignment. *Nat. Mater.* **2021**, 20, 624-631.

[42] Wan, S.; Li, Y.; Mu, J.; Aliev, A. E.; Fang, S.; Kotov, N. A.; Jiang, L.; Cheng, Q.; Baughman, R. H. Sequentially bridged graphene sheets with high strength, toughness, and electrical conductivity. *Proc. Natl. Acad. Sci. U. S. A.* **2018**, 115, 5359-5364.

[43] Podsiadlo, P.; Kaushik, A. K.; Arruda, E. M.; Waas, A. M.; Shim, B. S.; Xu, J.; Nandivada, H.; Pumplin, B. G.; Lahann, J.; Ramamoorthy, A.; Kotov, N. A. Ultrastrong and stiff layered polymer nanocomposites. *Science* **2007**, 318, 80-83.

[44] Ferrari, A. C.; Basko, D. M. Raman spectroscopy as a versatile tool for studying the properties of graphene. *Nat. Nanotechnol.* **2013**, 8, 235-246.

[45] Cançado, L. G.; Takai, K.; Enoki, T.; Endo, M.; Kim, Y. A.; Mizusaki, H.; Jorio, A.; Coelho, L. N.; Magalhães-Paniago, R.; Pimenta, M. A. General equation for the determination of the crystallite size La of nanographite by Raman spectroscopy. *Appl. Phys. Lett.* **2006**, 88, 163106.

[46] Zhang, Z.; Wang, Q.; Li, Y.; Wang, C.; Yang, X.; Shang, L. Cholesteric cellulose liquid crystal fibers by direct drawing. *Research* **2024**, 7, 0527.

[47] Wang, Z.; Zu, H.; Luo, Z.; Zhou, Y.; Ren, Y.; Zhang, H.; Zhang, Z.; Qian, W.; Fu, H.; Li, L.; Feng, H.; Chen, P.; Zhang, L.; Yuan, H.; Xia, J.; Zhao, X.; Li, S.; He, D. Polarization manipulation of electromagnetic interference shielding effectiveness utilizing graphene film-based metamaterials. *Nat. Commun.* **2026**, 17, 682.

[48] Hu, R.; Chen, Z.; Kim, S. K. Can thermal nonreciprocity help radiative cooling? *Research* **2024**, 7, 0563.

[49] Li, W.; Kong, L.; Xu, M.; Gao, J.; Luo, L.; Li, Y.; Wang, K.; Zhou, Y.; Li, L.; Wei, Y.; Zhang, X. Microsecond-scale transient thermal sensing enabled by flexible Mo1−xWxS2 alloys. *Research* **2024**, 7, 0452.

Electronic Supplementary Material

Scalable fiber-skeleton-reinforced graphene-assembled films enabling wash-durable wearable heating

Hao Yuan[1,2,§], Pengfei Chen[1,2,3,§], Xun Li[1,2,§], Xiaoxi Xu[1,2], Wei Qian[2], Huazhang Zhang[2], Zhe Wang[2,4], Huaqiang Fu[1,2], Dingsheng Wang[5,✉], and Daping He[1,2,3,✉]

[1] *School of Materials Science and Engineering, Wuhan University of Technology, Wuhan 430070, China*
[2] *Hubei Engineering Research Center of Radio Frequency Microwave Technology and Application, School of Physics and Mechanics, Wuhan University of Technology, Wuhan 430070, China*
[3] *State Key Laboratory of Silicate Materials for Architectures, Wuhan University of Technology, Wuhan 430070, China*
[4] *State Key Laboratory of Advanced Technology for Materials Synthesis and Processing, Wuhan University of Technology, Wuhan 430070, China*
[5] *Department of Chemistry, Tsinghua University, Beijing 100084, China*
[§] *Hao Yuan, Pengfei Chen, and Xun Li contributed equally to this work.*

✉Address correspondence to Dingsheng Wang. wangdingsheng@mail.tsinghua.edu.cn; Daping He. hedaping@whut.edu.cn

Supporting information to https://doi.org/10.26599/NR.2026.94908671

This file includes:

S1. GAFs prepared at different heat-treatment temperatures

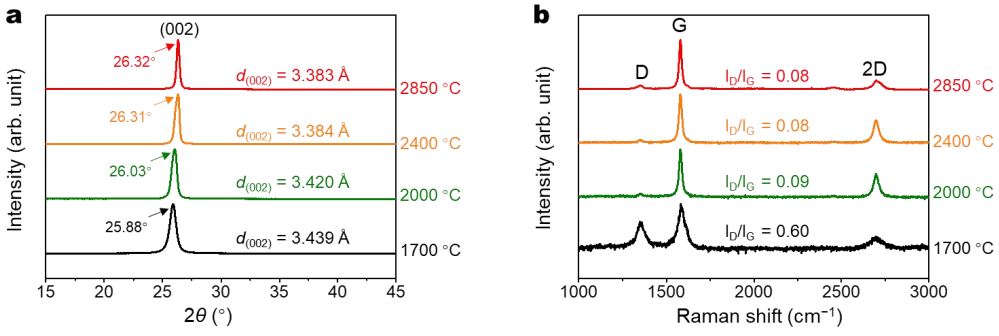

Figure S1. Structural evolution of GAFs prepared at different heat treatment temperatures. (a) XRD patterns, showing the shift of (002) peak toward higher angles, corresponding to a contraction of the interlayer spacing. (b) Raman spectra, exhibiting a significant drop in I_D/I_G ratio, indicating reduced lattice defects and enhanced graphitization at high temperatures.

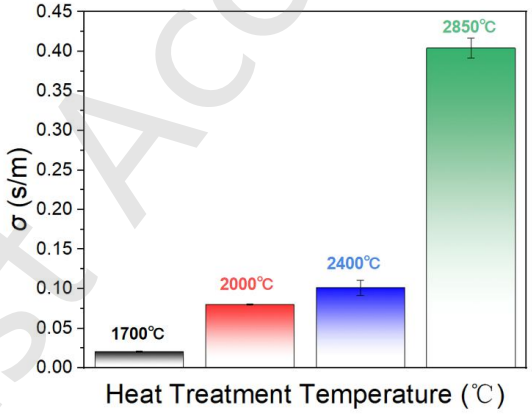

Figure S2. Electrical conductivity of GAFs prepared at different heat treatment temperatures. The GAFs treated at higher temperatures exhibit superior electrical conductivity, which is primarily attributed to the reduced lattice defects achieved during the high-temperature graphitization process.

S2. Electrothermal simulation

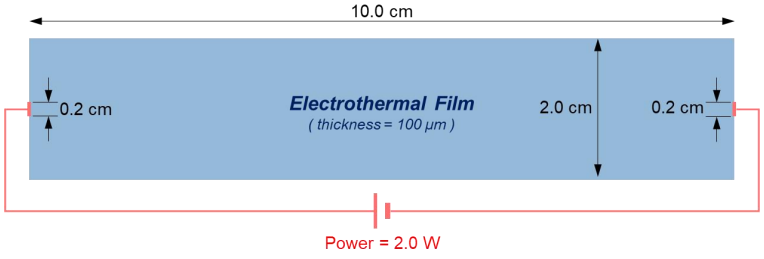

Figure S3. Electrothermal simulation model. The geometric model represents a film with in-plane dimensions of 10.0 cm × 2.0 cm and thickness of 100 μm. Electrodes with a contact width of 0.2 cm are set at the center of the left and right edges. The material property parameters employed are listed in Table S1. For the electrical boundary conditions, a constant input power of 2.0 W is applied across the electrodes. Thermal boundary conditions assume natural air convection on both the top and bottom surfaces, with a heat transfer coefficient h = 5.0 W/(m^2·K) and ambient temperature 20 °C.

Figure S4. Simulated current density distribution. Arrows indicate the direction of the current density vector, while the background color represents its magnitude. Despite the numerical value for J_{max} is different among different materials, the overall distribution remains consistent. A significant current concentration is observed near the electrodes, caused by the restricted contact width of the electrodes. According to Joule's law, these high-current-density regions correspond to the areas of concentrated heat generation.

Table S1. Materials properties employed in the electrothermal simulation and the calculated electrothermal performance metrics. The operating voltage is defined as the voltage required to achieve an input power of 2.0 W. Temperature RMS represents the root-mean-square of the steady-state temperature distribution across the film plane, quantifying the degree of temperature non-uniformity. The response time is determined as the time constant extracted from an exponential fit of the transient average temperature curve, characterizing the speed of thermal response.

Material	Electric conductivity (S/m)	Thermal conductivity [W/(m·K)]	Volumetric heat capacity [J/(cm^3·K)]	Operating voltage (V)	Temperature RMS (°C)	Response time (s)
Nichrome	9.0×10^5	11.3	3.78	0.369	22.25	40.78
Stainless Steel	1.4×10^6	16.3	4.00	0.296	18.64	42.93
Tungsten	1.8×10^7	173.0	2.58	0.083	3.52	26.18
Copper	5.8×10^7	401.0	3.45	0.046	1.63	37.72
Carbon Fiber	0.1×10^6	100.0	1.25	1.108	5.61	13.64
GAF	0.4×10^6	1000.0	1.12	0.554	0.52	15.01

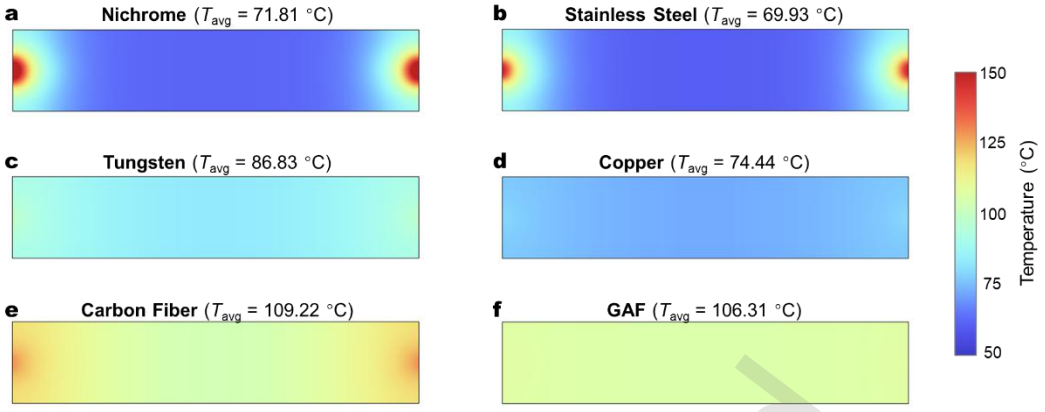

Figure S5. Transient temperature distributions at 30 s for electrothermal films of different materials. The average temperature (T_{avg}) is indicated in each panel.

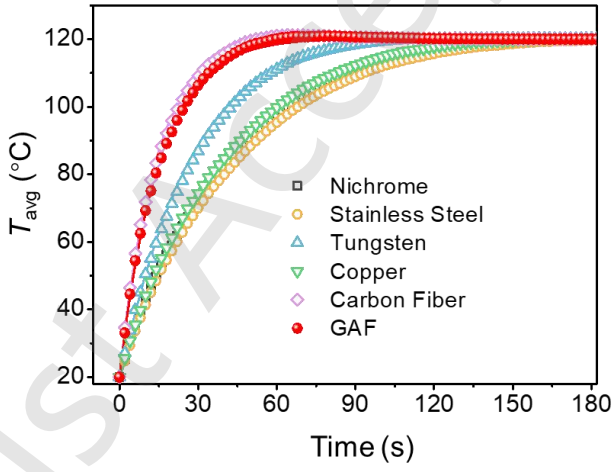

Figure S6. Simulated transient average temperature curves for electrothermal films of different materials.

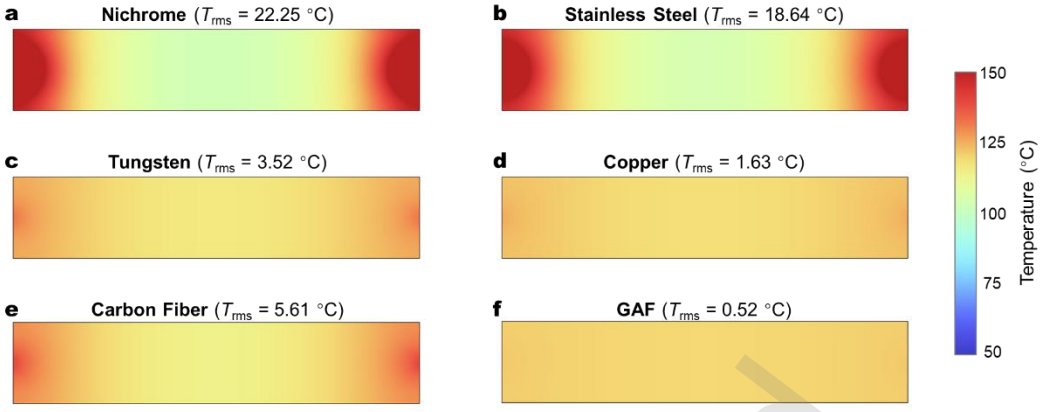

Figure S7. Steady-state temperature distributions for electrothermal films of different materials. The degree of temperature non-uniformity is quantified by the root-mean-square temperature (T_{rms}), as indicated in each panel.

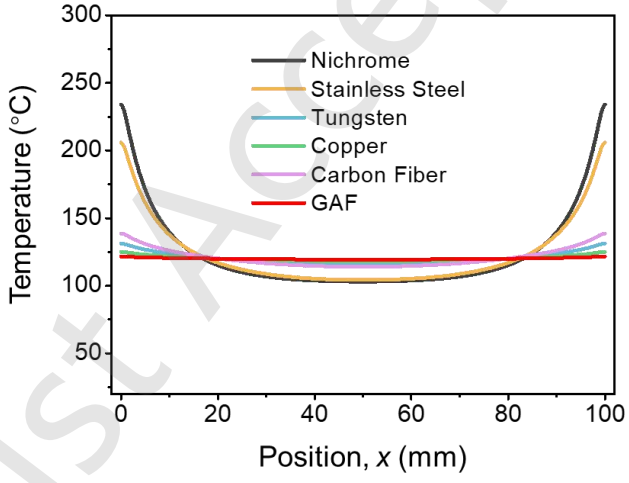

Figure S8. Steady-state temperature distributions along the horizontal axis of symmetry for the electrothermal films of different materials.

S3. Supplementary characterizations

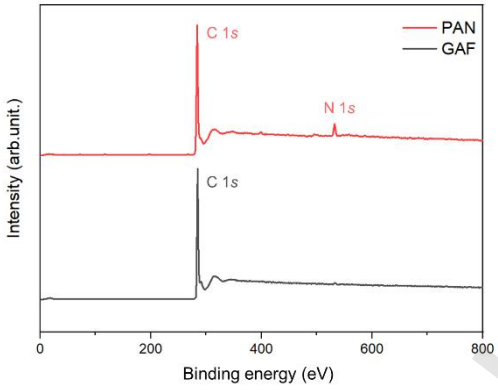

Figure S9. XPS spectra of the pristine PAN fiber precursor and the fiber-reinforced GAF after graphitization at 2850 °C, demonstrating the nearly complete elimination of nitrogen.

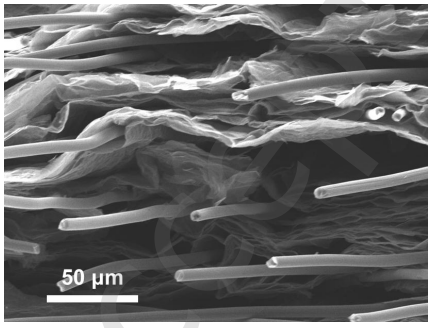

Figure S10. SEM image of the post-tensile fracture surface of fiber toughened GAF showing prominent fiber pull-out.

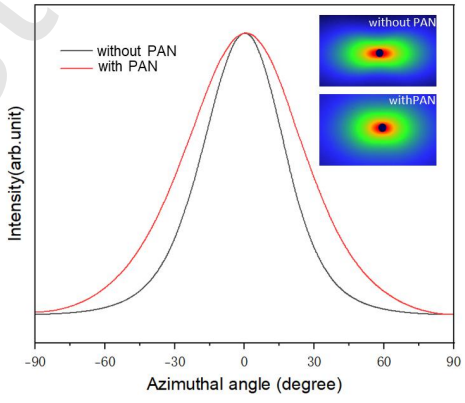

Figure S11. 2D SAXS patterns (insets) and the corresponding azimuthal intensity profiles of the pure GAF and the fiber-reinforced GAF. The broader distribution for the fiber-reinforced sample indicates a slight local perturbation of the parallel stacking induced by the intercalated carbon fibers.

S4. Heating elements with various geometric designs

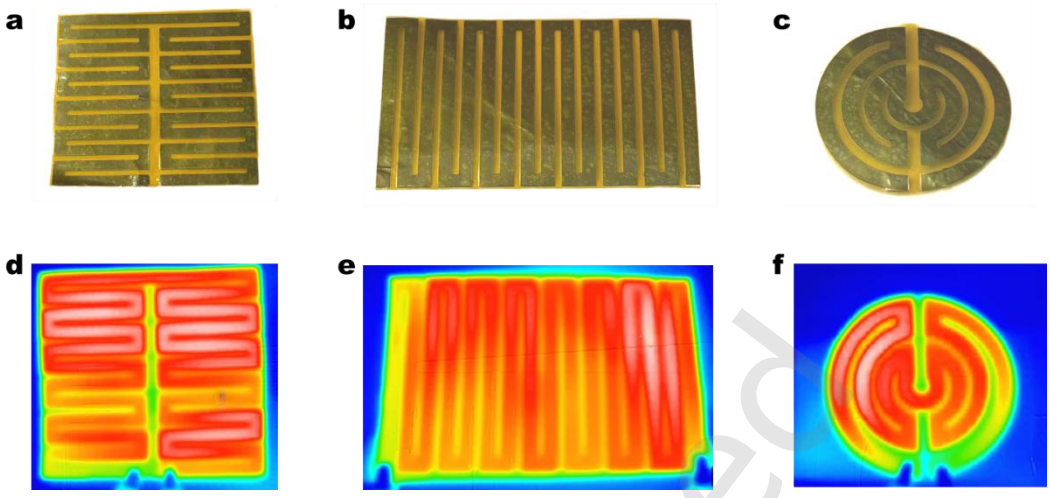

Figure S12. Optical photographs and infrared thermal images of GAF-based heating elements with various geometric designs. The GAF heating layer is encapsulated between two layers of yellow PI film. The samples correspond to (a, d) square, (b, e) rectangular, and (c, f) circular heating elements.

Table S2. Resistance, current and temperature of GAF-based heating elements with various geometric designs under operating voltage of 5.0 V.

	Resistance (Ω)	Current (A)	Temperature (℃)
Square	2.27	2.20	49.7
Rectangle	2.45	2.04	46.4
Circular	1.56	3.21	70.1

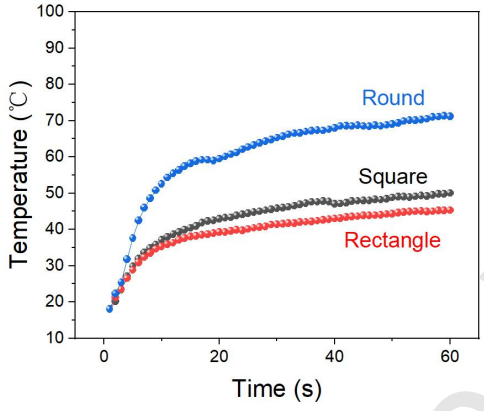

Figure S13. Time-dependent temperature profiles of GAF-based heating elements with various geometric designs under operating voltage of 5.0 V.